

Correlated hydrogen bonding fluctuations and vibrational cross peaks in *N*-methyl acetamide: Simulation based on a complete electrostatic density functional theory map

Tomoyuki Hayashi and Shaul Mukamel^{a)}*Department of Chemistry, University of California, Irvine, California 92697-2025*

(Received 5 June 2006; accepted 11 August 2006; published online 16 November 2006)

The coherent nonlinear response of the entire amide line shapes of *N*-methyl acetamide to three infrared pulses is simulated using an electrostatic density functional theory map. Positive and negative cross peaks contain signatures of correlations between the fundamentals and the combination state. The amide I-A and I-III cross-peak line shapes indicate positive correlation and anticorrelation of frequency fluctuations, respectively. These can be ascribed to correlated hydrogen bonding at C=O and N-H sites. The amide I frequency is negatively correlated with the hydrogen bond on carbonyl C=O, whereas the amide A and III are negatively and positively correlated, respectively, with the hydrogen bond on amide N-H. © 2006 American Institute of Physics. [DOI: 10.1063/1.2348865]

I. INTRODUCTION

Vibrational spectra are sensitive to the local solvent environment; frequency shifts with respect to the gas phase provide information about the average structure, whereas the line shapes reflect dynamical fluctuations. The amide I infrared absorption band of peptides which originates from the stretching motion of the C=O bond (coupled to N-H bending and C-H stretching) provides a useful indicator of secondary structure changes because of its sensitivity to hydrogen bonding, dipole-dipole interactions, and peptide backbone geometry. Coherent ultrafast vibrational spectroscopy is a powerful tool for probing molecular structure and dynamics in the condensed phase.¹⁻¹³ The anharmonicity and vibrational relaxation were probed in the first two-dimensional (2D) IR measurements of peptides.¹⁴ Extensive studies performed on a small and flexible peptide, trialanine, yielded the Ramachandran angles in good agreement with NMR.^{8,9} For larger peptides, 2D IR has been used to relate certain features in the spectra to typical structural motifs such as α helix, 3_{10} helix, and β sheet¹⁴⁻¹⁷ and identify distinct intramolecular hydrogen bonding patterns.¹⁸ Water is critical for protein-ligand and protein-protein interactions.¹⁹ Water in the protein solvation shell has different hydrogen-bond kinetics.^{20,21} Specific intermolecular hydrogen bonding patterns can activate protein functionalities in water.²²

The cross peak of amide A and I stretch vibrations has been observed.^{23,24} The simulation of cross peaks requires the modeling of the frequency fluctuations of amide II, III, and A modes induced by solvent and the protein environment. Several studies were carried out for the amide frequency fluctuations of *N*-methyl acetamide²⁵⁻²⁸ (NMA). Repeated *ab initio* calculations of the NMA-3H₂O clusters in which geometry was obtained from molecular dynamics (MD) trajectories in dielectric continuum reproduced the sol-

vent peak shifts of amide fundamentals from the gas phase,²⁵ but sampling enough statistics for calculating the dynamical infrared band shapes is prohibitively expensive. Empirical correlation between the amide I harmonic frequency and C=O bond length obtained from Hartree-Fock NMA-*n*H₂O cluster calculations^{26,27} was successfully applied for the amide I mode. Empirical correlations between the amide harmonic frequencies and the electrostatic potentials at several atomic positions based on density functional theory (DFT) calculations were also used in calculations of infrared spectra.²⁸ Anharmonicity fluctuations which are required for simulating coherent infrared signals were not studied so far.

We have simulated the linear infrared line shape of all amide modes (III, II, I, and A) in NMA (Ref. 29) using a complete electrostatic DFT map (EDM) of the fundamental and anharmonicity frequency fluctuations. The map provides the entire fluctuating Hamiltonian required for simulations of nonlinear spectra (fundamental, overtone, combination frequencies, and transition moments) from first principles, and incorporates high (up to fourth order) derivatives of the electrostatic potential, which were found crucial.^{29,30} An anharmonic vibrational Hamiltonian for the amide I, II, III, and A modes of NMA was recast in terms of the 19 components of an external electric field and its first and second derivative tensors (Electrostatic DFT map), calculated at the DFT [BPW91/6-31G(*d,p*)] level. Four amide fundamental frequencies and their combination and overtone frequencies, obtained by diagonalizing the Hamiltonian for the sixth order DFT anharmonic vibrational potential in different nonuniform electric fields, were parametrized in terms of these electrostatic components. The fluctuating Hamiltonian was calculated by using this map together with the fluctuating solvent electric field obtained from MD simulations in TIP3 water. The amide I and II anharmonicities are in agreement with a recent photon echo measurements of amide I and II of NMA.³¹

In a model study of two coupled vibrations interacting

^{a)}Electronic mail: smukamel@uci.edu

TABLE I. Statistics of 13 vibrational eigenstates of NMA amide I, II, III, and A modes in TIP3 water $\langle\omega\rangle$, ω_{gas} , $\Delta\omega$, and $\langle\delta\omega^2\rangle$ represent the average frequency, gas phase frequency, solvent shift from the gas phase, and variance, respectively. κ is the line broadening parameter [Eq. 8.50 of Ref. 36].

State	Description	$\langle\omega\rangle$	ω_{gas}	$\Delta\omega$	$\langle\delta\omega^2\rangle$	κ
1 Amide III	C–N–H bend, C–N stretching	1292.3	1259	+33	140	1.62
2 Amide II	C–N–H bend, C–N stretching, methyl deformation	1514.7	1500	+15	147	4.32
3 Amide I	Mostly C=O stretch	1669.4	1728	–59	266	0.75
4 Amide A	Mostly N–H stretch	3447.3	3498	–51	215	0.61
5 III \times 2		2574.7	2504	+71	727	
6 II \times 2		3016.3	2981	+35	555	
7 I \times 2		3325.0	3440	–115	1060	
8 III+II		2795.2	2758	+37	307	
9 III+I		2941.7	2971	–29	159	
10 II+I		3187.2	3230	–43	372	
11 III+A		4627.4	4737	–110	1800	
12 II+A		4892.5	4999	–107	1435	
13 I+A		5027.7	5223	–195	3104	

with a Brownian oscillator bath,³² distinct signatures of degrees of correlations between the two modes in the 2D IR spectra were found in the slow to the intermediate bath time scale regime. Correlations between different amide modes can provide more information about the protein structure and dynamics by examining the cross-peak line shapes. The correlation between the fundamental frequencies of two vibrations and their combination frequency is particularly interesting. Strong correlations of amide fluctuations²⁹ can be related to the solvent and hydrogen-bond dynamics.

In this paper we investigate the sensitivity of the amide cross peaks to these correlations by calculating the band shapes of amide I-III and amide I-A cross peaks. In order to establish the connection between hydrogen bonding dynamics and the amide frequency fluctuations, the hydrogen bonding configurations were classified by employing the geometric hydrogen-bond criteria. The correlation of the hydrogen bonding dynamics at the carbonyl oxygen (C=O) and amide hydrogen (N–H) sites of NMA was calculated.

The fluctuating Hamiltonian is described in Sec. II. The three-pulse coherent infrared spectra in the $\mathbf{k}_i = -\mathbf{k}_1 + \mathbf{k}_2 + \mathbf{k}_3$ and $\mathbf{k}_{\text{iii}} = \mathbf{k}_1 + \mathbf{k}_2 - \mathbf{k}_3$ directions (\mathbf{k}_1 , \mathbf{k}_2 , and \mathbf{k}_3 are the three incident pulse wave vectors) are simulated in Sec. II. Different degrees of correlations between the amide modes are investigated, and their signatures in the cross-peak line shapes are described. Hydrogen-bond dynamics at the carbonyl oxygen and amide hydrogen sites is analyzed and connected to the amide fluctuations in Sec. IV. The results are discussed in Sec. V.

II. FLUCTUATING HAMILTONIAN FOR THE ENTIRE AMIDE BAND

The Hamiltonian for the four coupled amide vibrations was obtained using the electrostatic DFT map reported earlier.²⁹ The map was constructed from the eigenstate calculation of the sixth order anharmonic vibrational Hamiltonian of the NMA monomer by varying the external electric field, its gradient, and second derivative tensors. The anhar-

monic vibrational Hamiltonian in the presence of nonuniform external field was calculated with all five normal modes at the BPW91/6-31+G(*d,p*) level³³ using our modified GAUSSIAN 03 code³⁴ (see Appendix A of Ref. 30). The frequencies ω_ν and transition dipoles $\mu_{\nu\nu'}$ were expanded to quadratic order in the electric field and its gradient tensor:

$$\omega_\nu = \Omega_{\text{gas}}^\nu + \sum_\alpha \Omega_\alpha^\nu E_\alpha + \frac{1}{2} \sum_{\alpha\beta} \Omega_{\alpha,\beta}^\nu E_\alpha E_\beta, \quad (1)$$

$$\mu_{\nu\nu'} = M_{\text{gas}}^{\nu\nu'} + \sum_\alpha M_\alpha^{\nu\nu'} E_\alpha + \frac{1}{2} \sum_{\alpha\beta} M_{\alpha,\beta}^{\nu\nu'} E_\alpha E_\beta.$$

Here α and β denote the 19 independent Cartesian components ($x, y, z, xx, yy, zz, xy, xz, yz, xxx, \dots, xyz$) in the molecular coordinate system (Fig. 2 of Ref. 29). ν and ν' run over 14 vibrational eigenstates (Table I) of ground state, four amide fundamentals (III, II, I, and A), first overtones of amide III, II, and I, and the combination states of amide III, II, I, and A. The EDM for the vibrational frequency and transition dipole moments is given in Tables X and XI in supporting information of Ref. 29.

The electric field and its derivatives are obtained by least-squares fits of the electric fields at sampling grid generated by water molecules within 12.0 Å radius calculated from a MD trajectory. We used 69 sampling points which cover the areas of transition charge densities (TCDs) of amide modes I, II, and A (Figs. 3 and 5 of Ref. 29). MD simulations were performed using the CHARMM force field³⁵ for NMA and 1000 TIP3 water molecules. Simulation details are given in Ref. 29. The average frequencies ($\langle\omega\rangle$), gas phase frequencies ω_{gas} , solvent shifts ($\Delta\omega \equiv \omega_{\text{gas}} - \langle\omega\rangle$), variances ($\Delta^2 \equiv \langle\delta\omega^2\rangle$), and line broadening parameter κ [Eq. (8.50) of Ref. 36] of the 13 eigenstates of NMA in water are tabulated in Table I. The amide III, I, and A modes are in the intermediate bath region ($\kappa = 1.62, 0.75, 0.61$) and amide II mode is close to the fast bath limit ($\kappa = 4.32$). The cross-peak band shape should depend on degree of correlation in the slow to the intermediate bath limit.³² Our simulation does not

TABLE II. Fluctuation amplitudes (Δ_{ii}) of the 13 amide states in cm^{-1} and their correlations (η_{ij}) with the fundamental fluctuations.

	1	2	3	4	5	6	7	8	9	10	11	12	13
Δ_{ii}	11.8	12.1	16.3	14.6	27.0	23.6	32.6	17.5	12.6	19.3	42.4	37.9	55.7
η_{11} (III)	1.00	0.60	-0.71	-0.52	0.96	0.55	-0.71	0.76	0.63	-0.24	-0.38	-0.52	-0.81
η_{12} (II)	...	1.00	-0.16	-0.69	0.47	1.00	-0.14	0.95	0.31	0.52	-0.54	-0.42	-0.66
η_{13} (I)	1.00	0.16	-0.69	-0.12	1.00	-0.31	-0.45	0.75	-0.14	0.07	0.45
η_{14} (A)	1.00	-0.45	-0.70	0.10	-0.74	-0.34	-0.36	0.95	0.93	0.92

include vibrational lifetime broadening (population relaxation).

III. CROSS-PEAK LINE SHAPES IN COHERENT INFRARED SPECTRA

The frequency-frequency correlation function of two vibrational transitions is given by

$$C_{ij}(t) \equiv \langle \delta\omega_i(0)\delta\omega_j(t) \rangle = \eta_{ij}\Delta_{ii}\Delta_{jj}\bar{C}_{ij}(t) \quad (i \neq j), \quad (2)$$

where $\Delta_{ii} \equiv \sqrt{\langle \delta\omega_i^2 \rangle}$ is a fluctuation amplitude, \bar{C}_{ij} is a normalized correlation function [$\bar{C}_{ij}(0)=1$], and $\eta_{ij} \equiv \langle \delta\omega_i\delta\omega_j \rangle / \sqrt{\langle \delta\omega_i^2 \rangle \langle \delta\omega_j^2 \rangle}$ is the correlation coefficient which varies between 1 (full correlation), 0 (no correlation), and -1 (anticorrelation). Δ_{ii} and η_{ij} are tabulated in Table II. The two bending (amide II and III) fundamentals are negatively correlated with the amide A fundamental. The two stretch (amide I and A) fundamentals are positively correlated. When two fundamental fluctuations are positively correlated, both frequencies are expected to be correlated with their combination frequency. The amide bending (III and II) fundamentals and their combination state (III+II) are positively correlated (0.76 and 0.95). The amide stretch (I and A) fundamentals and their combination state (I+A) are positively correlated (0.45 and 0.92). When the two fundamental frequencies are anticorrelated, their combination frequency is expected to be anticorrelated with one of the two fundamental fluctuations. The I+III combination state has a negative correlation with the amide I fundamental (-0.45) and a positive correlation with the amide III fundamental (0.63). The I+II combination state is positively correlated with both amide I and II fundamentals.

To investigate the sensitivity of coherent infrared signals to these correlated frequency fluctuations, we have simulated the three-pulse infrared signal of NMA generated along $\mathbf{k}_i \equiv -\mathbf{k}_1 + \mathbf{k}_2 + \mathbf{k}_3$ and $\mathbf{k}_{iii} \equiv \mathbf{k}_1 + \mathbf{k}_2 - \mathbf{k}_3$ with zzzz polarization using the cumulant expansion of Gaussian fluctuations (CGF).³⁶ The corresponding response functions for the signals [$R_i(t_3, t_2, t_1)$ and $R_{iii}(t_3, t_2, t_1)$] in the rotating wave approximation (RWA) are given by the sum of Liouville space pathways (Fig. 4) [Eqs. (5.19) and (5.20) of Ref. 37].

The signals $S(\omega_1, t_2=0, \omega_3)$ and $S(t_1=0, \omega_2, \omega_3)$ are calculated by a two-dimensional Fourier transform with respect to the time variables t_1 and t_3 and t_2 and t_3 , respectively. To compute the amide I, II, and III cross peaks, the three incident pulses were, tuned to 1500 cm^{-1} with a rectangular bandwidth of $\pm 250 \text{ cm}^{-1}$. All energy levels within $1500 \pm 250 \text{ cm}^{-1}$ were included in the sums over states. \mathbf{k}_i signal ($|S_i(-\omega_1, t_2=0, \omega_3)|$) and two \mathbf{k}_{iii} signals ($|S_{iii}(\omega_1, t_2=0, \omega_3)|$ and $|S_{iii}(t_1=0, \omega_2, \omega_3)|$) are plotted on a logarithmic scales in Fig. 1. The diagonal and off-diagonal peaks are observed at $(-1670, 1670)$, $(-1515, 1515)$, $(-1293, 1293)$, $(-1515, 1670)$, $(-1293, 1670)$, and $(-1293, 1515)$ in $|S_i(-\omega_1, t_2=0, \omega_3)|$. $|S_{iii}(\omega_1, t_2=0, \omega_3)|$ has a similar peak pattern to $|S_i(-\omega_1, t_2=0, \omega_3)|$ with a different sign of ω_1 . In $|S_{iii}(\omega_1, t_2=0, \omega_3)|$, the cross peaks are observed at the two fundamental frequencies along the ω_1 and ω_3 axes, whereas in $|S_{iii}(t_1=0, \omega_2, \omega_3)|$, the cross peaks of two amide states are located at their combination frequencies along ω_2 .

The absorptive part of the \mathbf{k}_i signal $\text{Im}[S_i(\omega_1, t_2=0, \omega_3)]$ is displayed in Fig. 2. A slice of the spectra along ω_3 for a fixed ω_1 shows two peaks representing stimulated emission/ground state bleach and excited state absorption. We have defined the frequency difference between these peaks for ω_1 as the anharmonic shift. Anharmonic shifts for

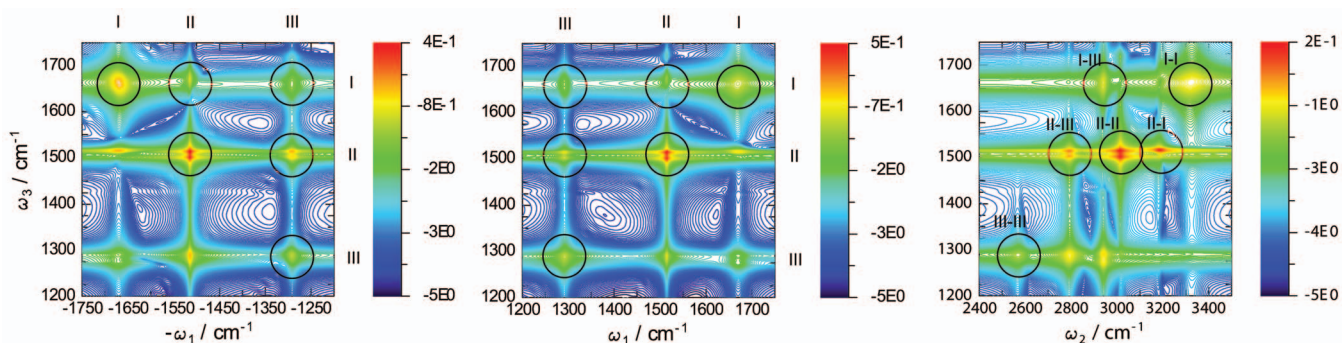


FIG. 1. (Color) Coherent infrared three-pulse signals of NMA in the cross-peak region of amide I, II, and III modes. Left panel: $\mathbf{k}_i = -\mathbf{k}_1 + \mathbf{k}_2 + \mathbf{k}_3$ signal ($\log|S_i(-\omega_1, t_2=0, \omega_3)|$); middle panel: $\mathbf{k}_{iii} = \mathbf{k}_1 + \mathbf{k}_2 - \mathbf{k}_3$ signal ($\log|S_{iii}(\omega_1, t_2=0, \omega_3)|$); and right panel: $\mathbf{k}_{iii} = \mathbf{k}_1 + \mathbf{k}_2 - \mathbf{k}_3$ signal ($\log|S_{iii}(t_1=0, \omega_2, \omega_3)|$). Peaks are marked by circles.

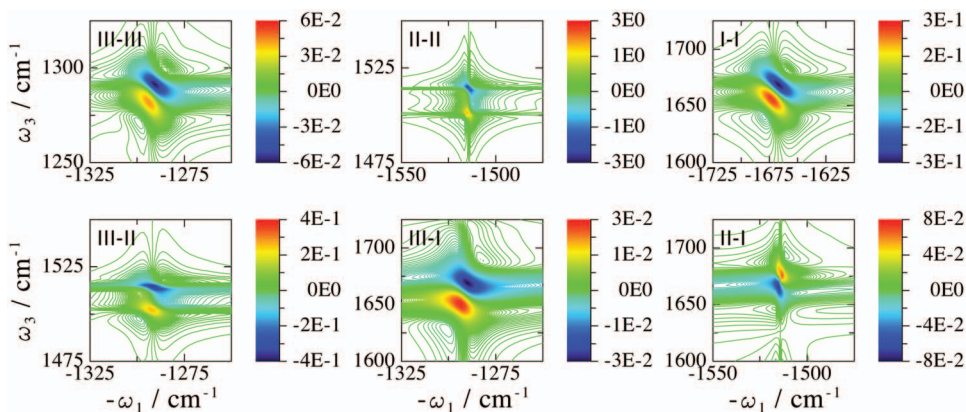


FIG. 2. (Color) Diagonal and off-diagonal peaks of the \mathbf{k}_i signal ($\text{Im}[S_i(-\omega_1, t_2=0, \omega_3)]$).

diagonal and off-diagonal peaks are tabulated with the calculated anharmonicities in Table III. The 17 cm^{-1} anharmonic shift of amide I diagonal peaks (the distance between the diagonal and the overtone peaks) was obtained in the simulation. The anharmonicity of a combination band ν is similarly defined as

$$\chi^{\nu_1, \nu_2} \equiv \omega^{\nu_1} + \omega^{\nu_2} - \omega^{\nu}, \quad (3)$$

where ν_1 and ν_2 are the two fundamental states (for an overtone we set $\nu_1 = \nu_2$). We found $\chi^{\text{I,III}} = 14.3 \text{ cm}^{-1}$.

In the simulations of the amide A cross peaks, the three incident pulses were tuned to $1500, 3400,$ and 1500 cm^{-1} with a 250 cm^{-1} bandwidth. The cross-peak region of amide A with other amide modes (I, II, and III) is shown in Fig. 3. The amide I-A cross peaks are most intense. The cross peaks in $|S_i(-\omega_1, t_2=0, \omega_3)|$ are broad along ω_2 due to larger fluctuation amplitudes of the amide A combination states (Table I).

We next discuss the sensitivity of the cross-peak band shape to the degree of correlation between amide modes. For the I-III cross peaks we find that the two fundamentals are anticorrelated and their combination state is correlated with amide I and anticorrelated with amide III. The I-A peaks probe the correlation of the hydrogen-bond dynamics at the two sites (C=O and N-H). Two cross peaks of amide I-III and of amide I-A in \mathbf{k}_i and \mathbf{k}_{iii} signals were calculated by varying η_{ij} in Eq. (2). In the calculation of amide I-A cross peak, the three incident pulses were tuned to $1670, 3400,$ and 1670 cm^{-1} with a smaller 100 cm^{-1} pulse width to avoid the overlap of the amide I-A cross peak with the II-A cross peak.

The response function (Chaps. 7 and 8 of Ref. 36) in the slow bath limit is

TABLE III. Overtone and combination band anharmonicities [χ^{ν_1, ν_2} in Eq. (3)] and anharmonic shift in the photon echo signal (Fig. 2) (in cm^{-1}).

	Anharmonicity	Anharmonic shift
I-I	14.3	17
II-II	13.0	13
III-III	10.7	13
I-II	-3.1	-15
I-III	19.7	22
II-III	11.0	12

$$R_i(t_3, t_2=0, t_1) \propto \exp \left[-\frac{1}{2} \Delta_{\alpha\alpha}^2 t_1^2 - \frac{1}{2} \Delta_{\beta\beta}^2 t_3^2 + \eta_{\alpha\beta} \Delta_{\alpha\alpha} \Delta_{\beta\beta} t_1 t_3 \right] \\ - \exp \left[-\frac{1}{2} \Delta_{\alpha\alpha}^2 t_1^2 - \frac{1}{2} (\Delta_{\alpha\alpha}^2 + \Delta_{\delta\delta}^2 - 2\eta_{\alpha\delta} \Delta_{\alpha\alpha} \Delta_{\delta\delta}) t_3^2 \right. \\ \left. - (\Delta_{\delta\delta}^2 - \eta_{\alpha\delta} \Delta_{\alpha\alpha} \Delta_{\delta\delta}) t_1 t_3 \right], \quad (4)$$

where $\Delta_{ij} \equiv C_{ij}(0)$. The first and the second terms correspond to the Feynman diagrams (a) and (b) in Fig. 4 with $t_2=0$ and give negative and positive peaks, respectively. Both terms are two-dimensional Gaussians in t_1 and t_3 . As $\eta_{\alpha\beta}$ is varied

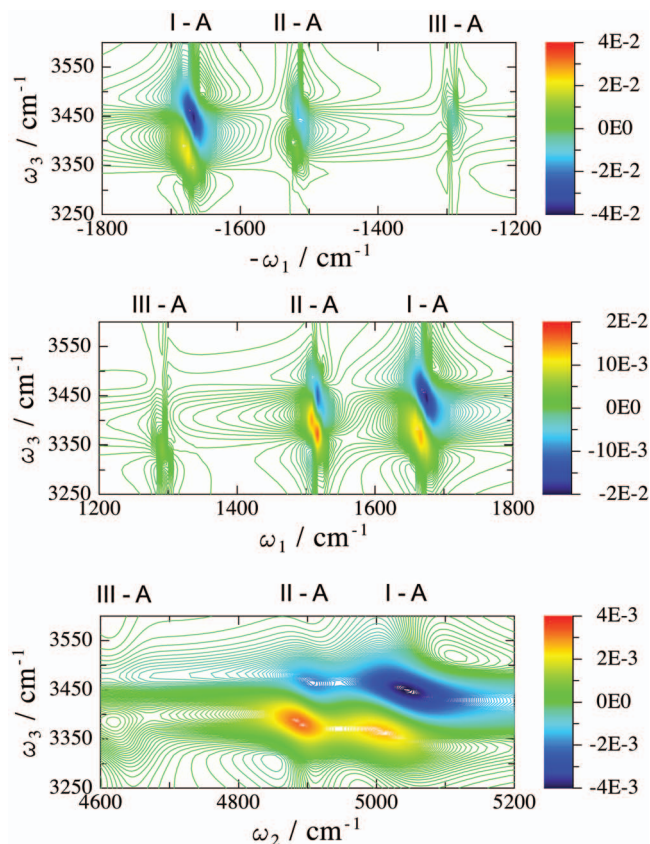


FIG. 3. (Color) Three-pulse signals of NMA in the cross-peak region of amide A with other amide modes. Top panel: \mathbf{k}_i signal ($\text{Im}[S_i(-\omega_1, t_2=0, \omega_3)]$); middle panel: \mathbf{k}_{iii} signal ($\text{Im}[S_{\text{iii}}(\omega_1, t_2=0, \omega_3)]$); and bottom panel: \mathbf{k}_{iii} signal ($\text{Im}[S_{\text{iii}}(t_1=0, \omega_2, \omega_3)]$).

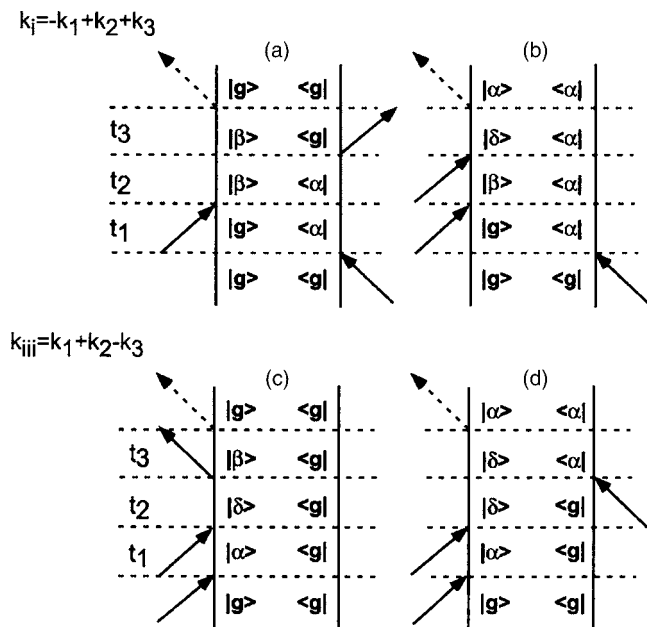


FIG. 4. Double-sided Feynman diagrams for the third order k_i and k_{iii} signals. α and β represent the fundamental states, and δ represents combination or overtone states. Pathways (a) and (c) give negative peaks, and pathways (b) and (d) give positive peaks.

from 1 to -1 , the width of the Gaussian along t_1 becomes narrower resulting in a broader signal in ω_1 . $\eta_{\alpha\beta}\Delta_{\alpha\alpha}\Delta_{\beta\beta}t_3$ determines the bandwidth in the antidiagonal direction. Positive correlation ($\eta > 0$) causes a narrow and intense band shape in this direction. As η is varied from $+1$ to -1 , the intensity of the positive peak becomes weaker.

The Gaussian width along t_3 ($\Delta_{\alpha\alpha}^2 + \Delta_{\delta\delta}^2 - 2\eta_{\alpha\delta}\Delta_{\alpha\alpha}\Delta_{\delta\delta}$) determines the elongation of the positive peak. The larger

Gaussian width (larger $\eta_{\alpha\delta}$) of the response function along t_3 causes the smaller width of the signal in ω_3 , resulting in the more horizontally elongated negative peak. Overall, the negative peak is stronger and narrower in the antidiagonal direction and the positive peak is stronger and horizontally elongated when the two fundamental fluctuations are positively correlated ($\eta_{\alpha\beta} > 0$).

For $R_{iii}(t_3, t_2=0, t_1)$ we have in the slow bath limit

$$R_{iii}(t_3, t_2=0, t_1) \propto \exp\left[-\frac{1}{2}\Delta_{\alpha\alpha}^2 t_1^2 - \frac{1}{2}\Delta_{\beta\beta}^2 t_3^2 - \eta_{\alpha\beta}\Delta_{\alpha\alpha}\Delta_{\beta\beta}t_1 t_3\right] - \exp\left[-\frac{1}{2}\Delta_{\alpha\alpha}^2 t_1^2 - \frac{1}{2}(\Delta_{\alpha\alpha}^2 + \Delta_{\delta\delta}^2 - 2\eta_{\alpha\delta}\Delta_{\alpha\alpha}\Delta_{\delta\delta})t_3^2 - (\Delta_{\alpha\alpha}^2 - \eta_{\alpha\delta}\Delta_{\alpha\alpha}\Delta_{\delta\delta})t_1 t_3\right]. \quad (5)$$

The first and the second terms correspond to diagrams (c) and (d) in Fig. 4 with $t_2=0$ and give negative and positive signals, respectively. The signal depends on two correlation factors ($\eta_{\alpha\beta}$ and $\eta_{\alpha\delta}$). Since the sign of the coupling term of the positive peak ($-\eta_{\alpha\beta}\Delta_{\alpha\alpha}\Delta_{\beta\beta}t_1 t_3$) is negative, the dependence of the negative peak on the correlation coefficient is opposite from $R_i(t_3, t_2, t_1)$. The negative peak is weaker and broader in the antidiagonal direction when the fundamental fluctuations are positively correlated ($\eta_{\alpha\beta} > 0$) and more intense in the case of the negative correlation ($\eta_{\alpha\beta} < 0$). The Gaussian width along t_3 ($\Delta_{\alpha\alpha}^2 + \Delta_{\delta\delta}^2 - 2\eta_{\alpha\delta}\Delta_{\alpha\alpha}\Delta_{\delta\delta}$) determines the elongation of the positive peak. As $\eta_{\alpha\delta}$ is varied from $+1$ to -1 , the positive peak becomes more elongated in ω_3 direction.

For $R_{iii}(t_3, t_2, t_1=0)$ we have in the slow bath limit

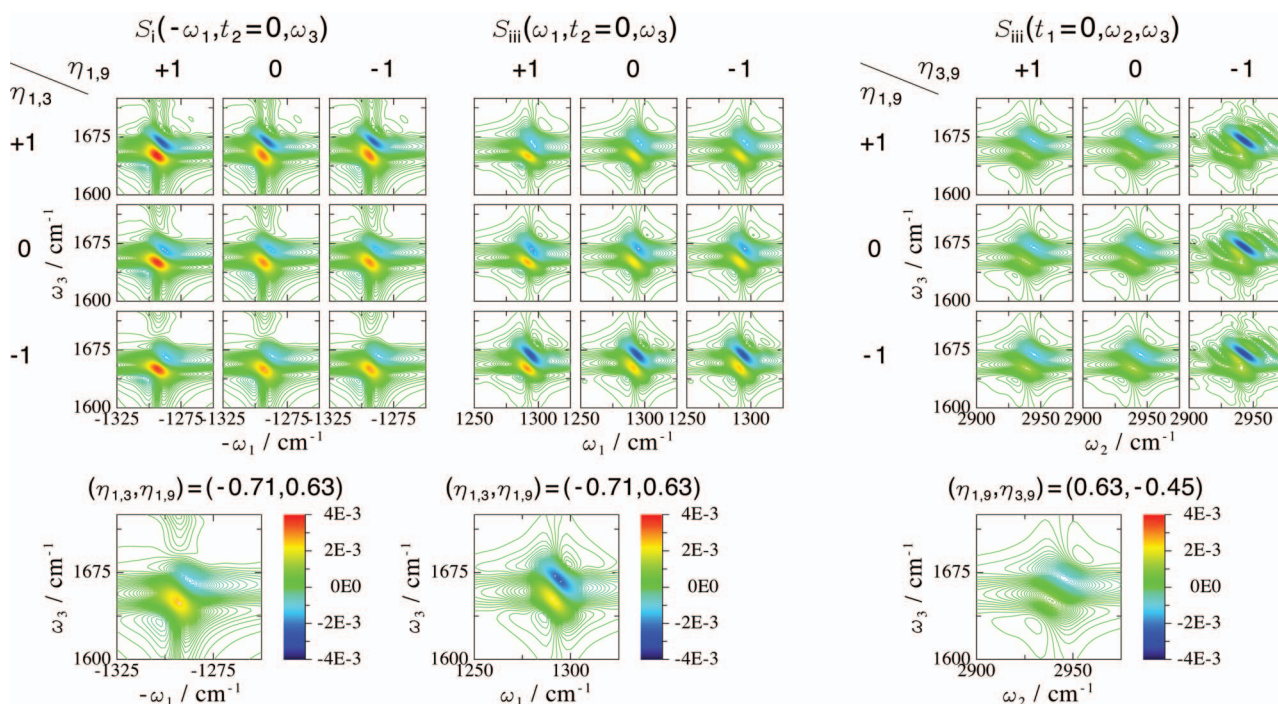


FIG. 5. (Color) Amide I-III cross-peak signals for different correlation coefficients. Left panels: $\text{Im}|S_i(\omega_1, t_2=0, \omega_3)|$ signal for different $\eta_{1,3}$ and $\eta_{1,9}$; middle panels: $\text{Im}|S_{iii}(\omega_1, t_2=0, \omega_3)|$ signal for different $\eta_{1,3}$ and $\eta_{1,9}$; and right panels: $\text{Im}|S_{iii}(t_1=0, \omega_2, \omega_3)|$ signal for different $\eta_{1,9}$ and $\eta_{3,9}$; and right panels: the bottom panels show the simulated signals.

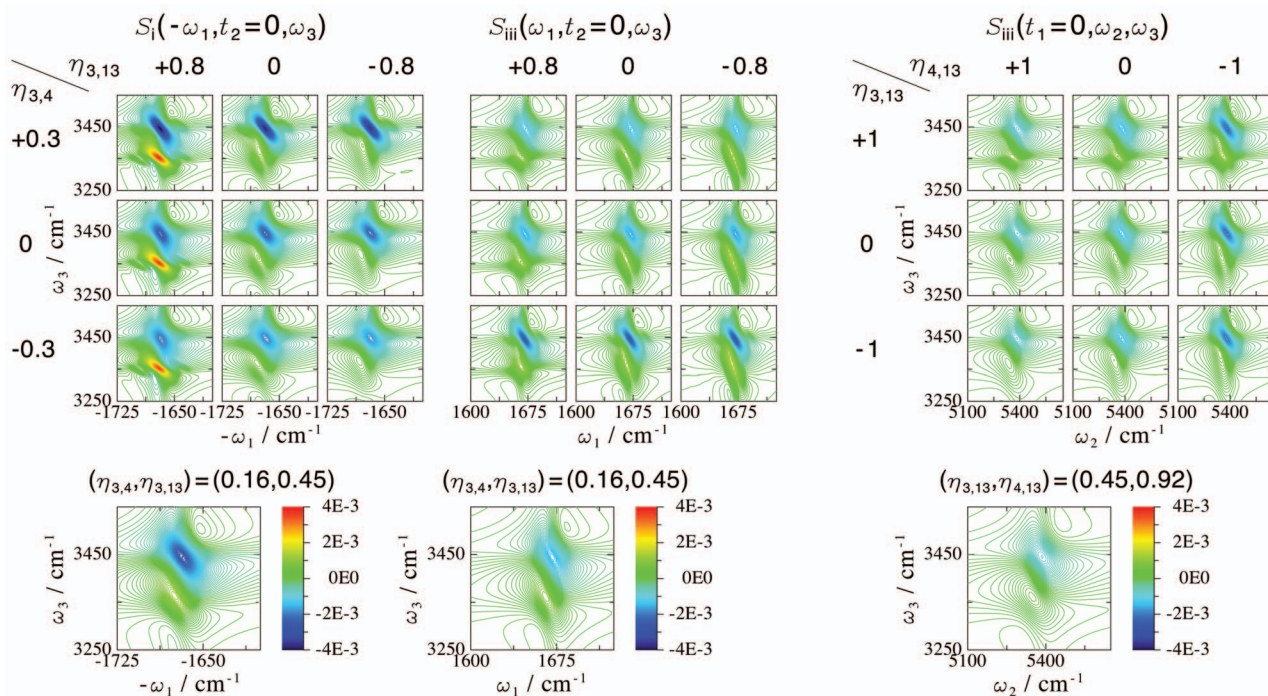


FIG. 6. (Color) Amide I-A cross-pick signals for different correlation coefficients. Left panels: $\text{Im}[S_i(-\omega_1, t_2=0, \omega_3)]$ signal for different $\eta_{3,4}$ and $\eta_{3,13}$; middle panels: $\text{Im}[S_{\text{iii}}(\omega_1, t_2=0, \omega_3)]$ signal for different $\eta_{3,4}$ and $\eta_{3,13}$; right panels: $\text{Im}[S_{\text{iii}}(t_1=0, \omega_2, \omega_3)]$ signal for different $\eta_{3,13}$ and $\eta_{4,13}$; and right panels: the bottom panels show the simulated signals.

$$R_{\text{iii}}(t_3, t_2, t_1 = 0)$$

$$\propto \exp \left[-\frac{1}{2} \Delta_{\delta\delta}^2 t_2^2 - \frac{1}{2} \Delta_{\beta\beta}^2 t_3^2 - \eta_{\beta\delta} \Delta_{\beta\beta} \Delta_{\delta\delta} t_2 t_3 \right] \\ - \exp \left[-\frac{1}{2} \Delta_{\delta\delta}^2 t_2^2 - \frac{1}{2} (\Delta_{\alpha\alpha}^2 + \Delta_{\delta\delta}^2 - 2\eta_{\alpha\delta} \Delta_{\alpha\alpha} \Delta_{\delta\delta}) t_3^2 \right. \\ \left. - (\Delta_{\delta\delta}^2 - \eta_{\alpha\delta} \Delta_{\alpha\alpha} \Delta_{\delta\delta}) t_2 t_3 \right]. \quad (6)$$

The first and the second terms correspond to the Feynman diagrams (c) and (d) in Fig. 4 with $t_1=0$ and give negative and positive signals, respectively. The signal depends on two correlation factors $\eta_{\alpha\delta}$ and $\eta_{\beta\delta}$ but not on the correlation between the two fundamentals $\eta_{\alpha\beta}$. When the fundamental β and the combination state δ are positively correlated, the negative signal becomes elongated along ω_2 . $\Delta_{\delta\delta}/\Delta_{\alpha\alpha} - \eta_{\alpha\delta}$ determines the elongation of the positive peak. As $\eta_{\alpha\delta}$ is varied from +1 to -1, the positive peak becomes weaker.

$\text{Im}[S_i(\omega_1, t_2=0, \omega_3)]$, $\text{Im}[S_{\text{iii}}(\omega_1, t_2=0, \omega_3)]$, and $\text{Im}[S_{\text{iii}}(t_1=0, \omega_2, \omega_3)]$ of the amide I-III cross peaks are plotted in Fig. 5 for various combinations of the correlation coefficients. Negative and positive peaks of $\text{Im}[S_i(\omega_1, t_2=0, \omega_3)]$ signal correspond to the two Liouville pathways (a) and (b) in Fig. 4 with $\alpha=1$, $\beta=3$, and $\delta=9$. The correlations between the amide I and III ($\eta_{1,3}$) contribute the negative band shape, and the correlation between the amide III and the combination state I+III ($\eta_{1,9}$) contributes to the positive band shape [Eq. (4)]. The height of the negative peak [path (a)] becomes smaller as $\eta_{1,3}$ is varied from +1 to -1 but does not depend significantly on $\eta_{1,9}$. The bandwidth also becomes broader with smaller $\eta_{1,9}$. On the other hand, the posi-

tive peak [path (b)] becomes weaker and broader as $\eta_{1,9}$ goes from the full correlation (+1) to anticorrelation (-1). The elongation of the positive (b) band shape also changes with $\eta_{1,9}$. As $\eta_{1,9}$ goes from +1 to -1, the positive peak becomes elongated more in ω_3 direction. The simulation (anticorrelated $\eta_{1,3}=-0.71$ and correlated $\eta_{1,9}=0.63$) gives weaker signals than when both are fully correlated.

The negative and positive peaks of $\text{Im}[S_{\text{iii}}(\omega_1, t_2=0, \omega_3)]$ correspond to Liouville pathways (c) and (d) in Fig. 4 with $\alpha=1$, $\beta=3$, and $\delta=9$. Our analysis in the slow bath limit also suggests that the correlations between the amide I and III ($\eta_{1,3}$) contribute the negative band shape and the correlation between the amide III and the combination state I+III ($\eta_{1,9}$) contributes to the positive band shape [Eq. (5)]. However, the band shape dependence on the two correlations $\eta_{1,3}$ and $\eta_{1,9}$ is different from the \mathbf{k}_i signal ($\text{Im}[S_i(\omega_1, t_2=0, \omega_3)]$) (Fig. 5). The intensity of the negative peak from path (c) becomes larger and its bandwidth becomes larger as $\eta_{1,3}$ goes from +1 to -1, which is opposite to \mathbf{k}_i signal. The positive signal from path (d) behaves similarly to \mathbf{k}_i signal. In path (c) of the Feynman diagram for \mathbf{k}_{iii} signal shown in Fig. 4, dephasing of both amide I and amide III fundamentals adds up in the ket resulting in the broadest negative peak with the full correlated case ($\eta_{1,3}=+1$). The simulation (anticorrelated $\eta_{1,3}=-0.71$ and correlated $\eta_{1,9}=0.63$) gives stronger signals than when both are fully correlated.

$\text{Im}[S_{\text{iii}}(t_1=0, \omega_2, \omega_3)]$ of the amide I-III cross peaks changes with varying $\eta_{1,9}$ (amide III and amide III+I) and $\eta_{3,9}$ (amide I and amide III+I). As suggested by Eq. (6), the negative peak from path (c) becomes stronger as $\eta_{1,9}$ is var-

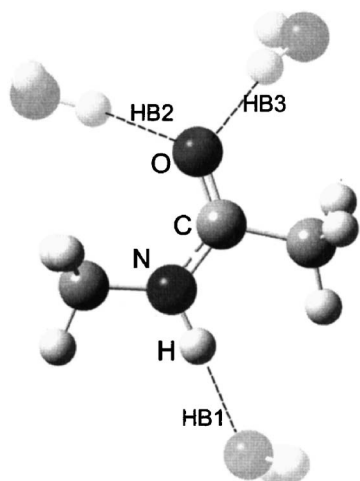


FIG. 7. The three possible hydrogen bondings in NMA. The hydrogen bond to N–H is labeled as HB1, and the two hydrogen bonds to C=O are labeled as HB2 and HB3.

ied from +1 to -1 . The intensity of the positive peak from path (d) increases as $\eta_{3,9}$ goes from the full correlation (+1) to anticorrelation (-1).

$\text{Im}[S_i(\omega_1, t_2=0, \omega_3)]$, $\text{Im}[S_{\text{iii}}(\omega_1, t_2=0, \omega_3)]$, and $\text{Im}[S_{\text{iii}}(t_1=0, \omega_2, \omega_3)]$ of the I-A cross peaks are plotted in Fig. 6 for various combinations of the correlation coefficients. $\text{Im}[S_i(\omega_1, t_2=0, \omega_3)]$ changes with varying $\eta_{3,4}$ (amide I and A) and $\eta_{3,13}$ (amide I and amide I+A). Negative and positive peaks are caused by the pathways (a) and (b) in Fig. 4 with $\alpha=3$, $\beta=4$, and $\delta=13$. The positive and negative peaks behave in a similar way as the amide III-I cross peak. The negative peak becomes weaker as $\eta_{3,4}$ goes from +0.3 to -0.3 . The positive peak becomes weaker as $\eta_{3,13}$ goes from +0.8 to -0.8 . The elongation of the positive peak changes more prominently than amide III-I cross peak. The positive peak becomes more elongated in ω_3 direction when $\eta_{3,4}$ is positive and $\eta_{3,13}$ is negative. Correlated $\eta_{3,4}$ and $\eta_{3,13}$ found in our simulation (0.16 and 0.45) enhance the negative and positive peaks compared to both noncorrelated.

$\text{Im}[S_{\text{iii}}(\omega_1, t_2=0, \omega_3)]$ of the I-A cross peaks also depends on the same nine different combinations of the correlation coefficients. Negative and positive peaks are caused by pathways (c) and (d) in Fig. 4 with $\alpha=3$, $\beta=4$, and $\delta=13$. The negative peak becomes stronger as $\eta_{3,4}$ goes from +0.3 to -0.3 , which is opposite to the trend in \mathbf{k}_i signal. The positive peak becomes stronger as $\eta_{3,13}$ goes from +0.8 to -0.8 . The elongation of the positive peak changes more prominently than amide I-A cross peak. The positive peak becomes more elongated along ω_3 when $\eta_{3,4}$ is positive and $\eta_{3,13}$ is negative. In path (c) of the Feynman diagram for \mathbf{k}_{iii} shown in Fig. 4, dephasing of both amide I and amide A fundamentals adds up in the ket resulting in the broadest negative peak with the full correlated case ($\eta_{3,4}=+1$). Correlated $\eta_{3,4}$ and $\eta_{3,13}$ found in the simulation (0.16 and 0.45) give weaker signals than when both are noncorrelated.

$\text{Im}[S_{\text{iii}}(t_1=0, \omega_2, \omega_3)]$ peaks of the I-A cross peaks depend on $\eta_{1,9}$ (amide I and amide I+A) and $\eta_{3,9}$ (amide I and amide I+A). The negative (c) peak intensity becomes larger

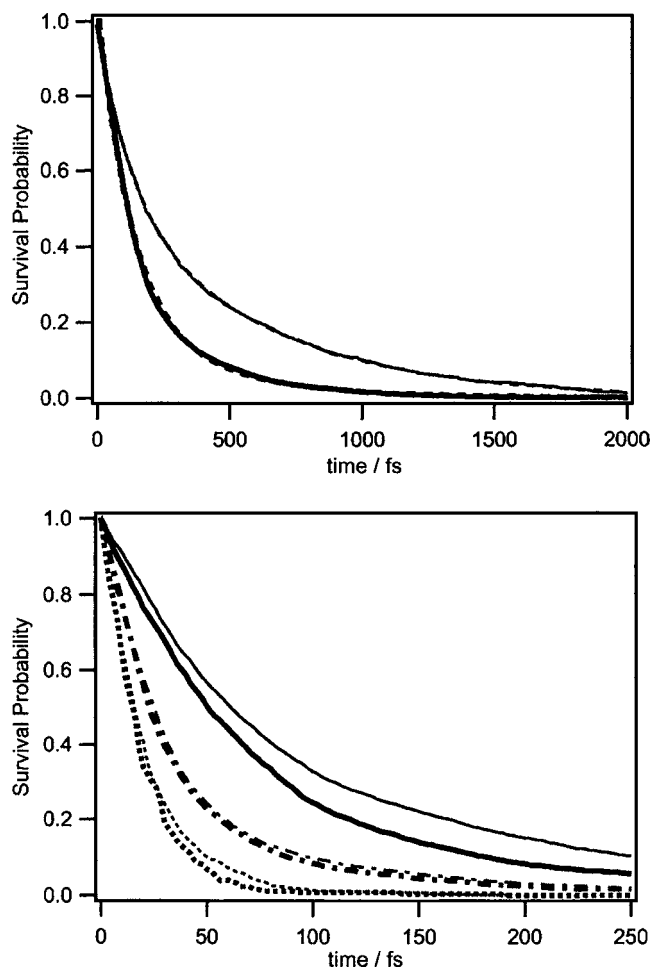


FIG. 8. Top: Survival probability histogram of the hydrogen bond of N–H and C=O sites. Thin line: N–H, thick line: C=O. Dashed lines represent the double exponential fits. Bottom: Survival probability histogram of the six hydrogen-bond configurations (Table V). Thin solid: 1, thick solid: 2, thin dash dotted: 3, thick dash dotted: 4, thin dashed: 5, and thick dashed: 6.

as $\eta_{1,9}$ goes from the full correlation (+1) to anticorrelation (-1). In the positive (d) signal, the positive peak intensity becomes larger as $\eta_{3,9}$ goes from +1 to -1 .

IV. HYDROGEN-BOND DYNAMICS

The signatures of positive correlation of the amide I and A and anticorrelation of the amide I and III frequencies in the coherent infrared cross-peak line shapes were described in the previous section. To connect the correlated amide frequency fluctuations with the underlying hydrogen-bond dynamics, we have investigated the kinetics of the hydrogen-bond forming and breaking based on the same MD trajectory as described in Sec. II. Two sites of NMA can have hydrogen bonds with water (Fig. 7). The amide N–H and carbonyl C=O can form N–H \cdots H $_2$ O (HB1) and C=O \cdots H–OH (HB2 and HB3), respectively. The geometric hydrogen bonding criteria^{38–40} requiring the N–O (O–O) distance to be less than 3.5 Å and the O–N–H (O–O–H) and angle to be less than 30° were employed. If more than one (or two) hydrogen bonds to N–H (C=O) are found, only the shortest are accepted.

TABLE IV. Statistics of two hydrogen-bond dynamics on amide H (N–H) and carbonyl O (C=O) sites. $\langle N \rangle$ is the average number of hydrogen bonds. A_i and τ_i are the fitted parameters to the survival probability histogram with Eq. (9).

H bond	$\langle N \rangle$	τ (s)	A_1	A_2	τ_1	τ_2
C=O	1.747	219	0.856	0.193	128	421
N–H	0.737	336	0.437	0.566	116	571

Our simulations give for the average number of hydrogen bonds $\langle N_{CO} \rangle = 1.747$ and $\langle N_{NH} \rangle = 0.737$. The correlation coefficient

$$\chi_{NN} \equiv \langle \delta N_{NH} \delta N_{CO} \rangle / \sqrt{\langle \delta N_{NH}^2 \rangle \langle \delta N_{CO}^2 \rangle} \quad (7)$$

is 0.673. This positive correlation indicates that the hydrogen bond at one site favors hydrogen-bond formation at the other. This can be rationalized since hydrogen bond at one site creates an electric field parallel to the C=O or N–H bond, which stabilizes the other hydrogen bond. The positive correlation may be enhanced further since the hydrogen bond at one site polarizes the NMA by changing the electronic structure in a way that stabilizes the hydrogen-bond formation at the other site. This effect requires a polarizable force field which goes beyond the present fixed-charge classical MD simulation. Earlier study of bulk water also showed that the polarizability stabilizes the hydrogen bonds and increases the hydrogen-bond relaxation time.⁴¹ Two polarizable force fields of water gave two extreme (largest and smallest) vibrational bandwidths compared to two fixed-charge models.³⁰

The survival probability histogram of a hydrogen bond,

$$P(t) = 1 - \int_0^t n(\tau) d\tau, \quad (8)$$

where $n(\tau)$ is the lifetime distribution, is shown in Fig. 8. The lifetime is defined as a period between hydrogen-bond formation and breaking at the C=O or N–H site. The average number of hydrogen bonds, the integrated lifetime [$\tau \equiv \int_0^\infty dt P(t)$], and the following fit parameters

$$P(t) = A_1 \exp(-t/\tau_1) + A_2 \exp(-t/\tau_2) \quad (9)$$

are tabulated in Table IV. The hydrogen bond to N–H has a longer lifetime (336 fs) than to C=O (219 fs).

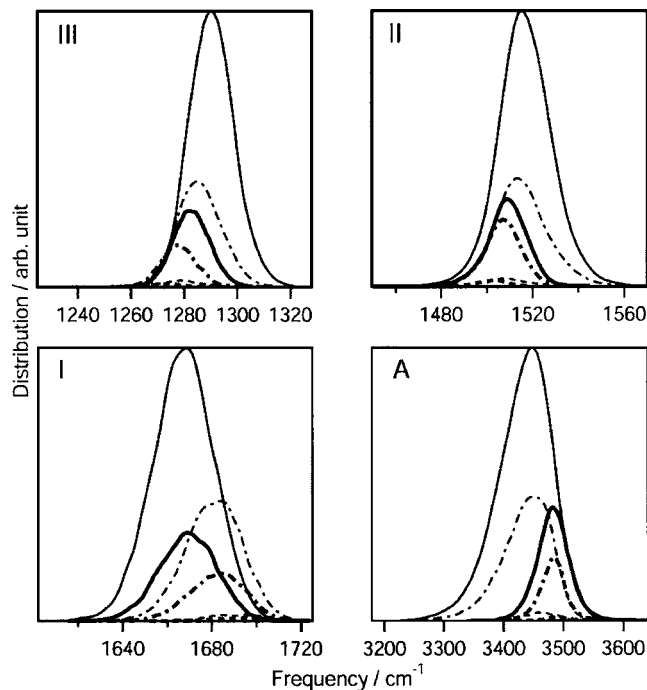


FIG. 9. Distribution of all amide fundamental frequencies for the six hydrogen-bond configurations (Table V). The integrated intensity of each curve give the abundance of each species. Thin solid: 1, thick solid: 2, thin dash dotted: 3, thick dash dotted: 4, thin dashed: 5, and thick dashed: 6.

We have classified the hydrogen-bond configuration into six species (n, m) with $n=0, 1, 2$ and $m=0, 1$ denoting the number of hydrogen bonds of C=O and N–H, respectively. The residence time in a given configuration was calculated from the MD trajectory, and survival probability histograms were constructed for each of the six configurations. Statistical data for these six configurations are given in Table V. The population P of each configuration was obtained by binning the snapshots. Configuration 1 (2,1) is most abundant followed by configurations 2 (2,0) and 3 (1,1) with one broken hydrogen bond on N–H and C=O. The average and standard deviation Δ of the four amide fundamental fluctuations are listed as well. The frequency distributions of the four amide fundamentals for the six configurations are given in Fig. 9. The amide I fundamental is sensitive to hydrogen bond on C=O. One hydrogen bond redshifts the frequency by 10 cm^{-1} and the second shifts it by another 22 cm^{-1} . The

TABLE V. Number of hydrogen bonds (N) to each site (N–H and C=O), population [P (%)], lifetime [τ (s)], average solvent frequency shift from the gas phase [$\langle \Delta\omega \rangle$ (cm^{-1})] and standard deviation [σ (cm^{-1})] of the amide fundamentals.

Configuration No.	N		P (%)	τ (fs)	Amide III		Amide II		Amide I		Amide A	
	C=O	N–H			$\langle \Delta\omega \rangle$	σ						
1	2	1	49.39	53.3	35	8.5	18	12.0	-62	13.7	-61	46.4
2	2	0	18.46	40.0	27	6.9	9	9.4	-61	12.8	-14	28.5
3	1	1	20.92	22.7	30	8.5	16	12.2	-49	12.9	-60	43.4
4	1	0	8.22	20.8	22	6.7	7	9.3	-47	12.4	-15	23.2
5	0	1	1.52	12.0	23	8.2	9	11.6	-38	12.1	-47	39.0
6	0	0	0.06	10.5	13	6.9	1	13.0	-37	12.0	-12	20.1
Average	1.747	0.737			33	11.8	14	12.1	-59	16.3	-51	14.7

TABLE VI. Degrees of correlation between hydrogen bondings ($\chi_{N\omega}^{\alpha i}$) at the two sites and the amide fundamental frequencies.

	Amide III	Amide II	Amide I	Amide A
C=O	0.304	0.106	-0.473	-0.028
N-H	0.364	0.306	-0.054	-0.430

amide I fundamental depends very weakly on the hydrogen bond to N-H ($<2\text{ cm}^{-1}$). The amide A fundamental depends mostly on the hydrogen bond to N-H ($40\text{--}50\text{ cm}^{-1}$ redshift). The shift due to hydrogen bond to C=O is less than 6 cm^{-1} . The amide II and III fundamentals are sensitive to both hydrogen bonds to N-H and C=O. The hydrogen bond to N-H blueshifts more (8 and 9 cm^{-1} for amide III and II; $2 \rightarrow 1$) than C=O (5 and 2 cm^{-1} for amide III and II; $3 \rightarrow 1$).

The degrees of correlation between the hydrogen bondings at the two sites and the amide frequencies,

$$\chi_{N\omega}^{\alpha i} \equiv \langle \delta N_{\alpha} \delta \omega_i \rangle / \sqrt{\langle \delta N_{\alpha}^2 \rangle \langle \delta \omega_i^2 \rangle}, \quad (10)$$

where $\alpha = \text{CO, NH}$ and $i = 1\text{--}4$, are listed in Table VI, which summarizes the sensitivity of the amide frequencies to hydrogen bonding. Hydrogen bonding formation on N-H blueshifted the bending frequencies (amide II and III) and redshifted the amide A frequencies. Hydrogen bonding on C=O redshifted the amide I frequencies. Positive correlation between the amide I and A and anticorrelation between the amide I and III (Table II) can be ascribed to the correlated hydrogen-bond dynamics at the two sites. The amide I is negatively correlated with the hydrogen bonding at the C=O site, and the amide A and III are negatively and positively correlated with the hydrogen bonding at N-H, respectively. The positive correlation of the two hydrogen-bond dynamics on C=O and N-H sites causes positive correlation between the amide I and A and negative correlation between the amide I and III fluctuations.

All amide fundamentals are shifted from the gas phase even without any hydrogen bonds (configuration 6) due to the reaction field (global solvent reorientation). The difference between the average solvent peak shifts, and the shifts of configuration 6 can be ascribed to the hydrogen bonds. The contributions of the reaction field and the hydrogen bonds to the frequency shifts are listed in Table VII. The global solvation and the hydrogen bonds have the largest contribution to amide I compared to the hydrogen bonds I (63% and 37%). The two contributions are comparable in amide III (39% and 61%) and amide A (24% and 76%).

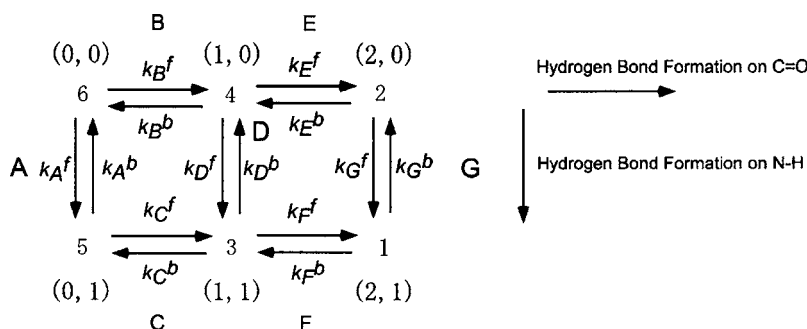


FIG. 10. Kinetic scheme for the six hydrogen bonding configurations (Table V). (n, m) represents the number of hydrogen bonds at C=O and N-H. Reactions A, D, and G form/break^b hydrogen bonds on N-H, while B, C, E, and F form/break^b hydrogen bonds on C=O.

TABLE VII. Contributions of solvation and the hydrogen bonding to the the solvent frequency shifts of the four amide fundamentals.

	Amide III	Amide II	Amide I	Amide A
Solvation	+13 (39%)	+0.5 (4%)	-37 (63%)	-12 (24%)
H bond	+20 (61%)	+13.5(96%)	-22 (37%)	-39 (76%)
Total	+33	+14	-59	-51

Solvation contributes less to amide II. Amide I is therefore most sensitive to solvent reorientation and amide II is sensitive exclusively to the hydrogen bonding.

The equilibrium constants for the seven hydrogen-bond forming reactions obtained from the equilibrium populations are given in Table VIII. Each configuration has two or three possible reactions (Fig. 10). The inverse of the lifetime (T) of each configuration is written as a sum of the rate constants for the possible reactions: $1/T_1 = k_A^f + k_B^f$, $1/T_2 = k_A^b + k_C^f$, $1/T_3 = k_B^b + k_D^f + k_E^f$, $1/T_4 = k_C^b + k_D^b + k_F^f$, $1/T_5 = k_E^b + k_G^f$, and $1/T_6 = k_F^b + k_G^b$. For each configuration, the ratio of the rate constants for possible reactions is calculated from the MD trajectory by counting the number of happened transitions for each reaction. The rate constants calculated from the lifetime and the branching ratio are tabulated in Table VIII. Free energies of the four major species 1, 2, 3, and 4 (98% of the population) are calculated from their equilibrium populations (Fig. 11). The stabilization free energy of the hydrogen-bond formation on N-H (ΔG_{NH}) is calculated as 0.55 kcal/mol from the free energy difference of configurations 3 and 4. We find the stabilization energy of the hydrogen-bond formation on C=O (ΔG_{CO}) to be 0.48 kcal/mol (free energy difference of configurations 2 and 4). *Ab initio* calculations of the NMA+water clusters in the gas phase showed much larger stabilization energies for the hydrogen bondings (7.5 kcal/mol for N-H and 9.6–9.8 kcal/mol for C=O).⁴¹ The additional stabilization energy when both hydrogen bonds at C=O and N-H are formed ($\Delta\Delta G$) has a following relation with the equilibrium constants:

$$\exp(-\Delta\Delta G/k_B T) = K_D/K_G = K_E/K_F. \quad (11)$$

This gives $\Delta\Delta G = 0.03\text{ kcal/mol}$. The correlated hydrogen-bond dynamics is determined by this small energy, and the multidimensional infrared spectroscopy should be sensitive to this small energy difference. A larger stabilization energy (-0.1 kcal/mol) was found in the gas phase *ab initio* cluster calculation when the three hydrogen bondings are formed.⁴¹

TABLE VIII. Reaction dynamics for hydrogen-bond breakings and forming.

Reaction	A	B	C	D	E	F	G
Equation constant K	2.59	14.0	13.8	2.54	2.25	2.36	2.67
Forming [k^f (ps ⁻¹)]	10.98	82.8	79.0	10.7	31.7	34.4	10.4
Breaking [k^b (ps ⁻¹)]	4.2	5.9	5.7	4.2	14.1	14.6	4.0

V. DISCUSSION

The three-pulse infrared spectra of the entire amide bands (amide I, II, III, and A) of NMA in the \mathbf{k}_i (three-pulse photon echo) and \mathbf{k}_{iii} directions were simulated. The amide cross-peak band shapes are sensitive to the correlated amide vibrations which are connected to the correlated hydrogen-bond dynamics at C=O and N-H. The spectral shapes of the three-pulse \mathbf{k}_i ($\text{Im}[S_i(-\omega_1, t_2=0, \omega_3)]$) and \mathbf{k}_{iii} ($\text{Im}[S_{iii}(\omega_1, t_2=0, \omega_3)]$ and $\text{Im}[S_{iii}(t_1=0, \omega_2, \omega_3)]$) signals are sensitive to the degrees of correlation between different amide states. Negative and positive peaks appear in all signals originated from different Liouville pathways involving two fundamental states and their combination state. States 1 (III), 3 (I), and 9 (III+I) are involved for amide I-III cross peaks and states 3 (I), 4 (A), and 13 (I+A) are involved for amide I-A cross peaks. The negative peaks of $\text{Im}[S_i(-\omega_1, t_2=0, \omega_3)]$ and $\text{Im}[S_{iii}(-\omega_1, t_2=0, \omega_3)]$ are sensitive to the correlation between the two fundamental frequency fluctuations ($\eta_{1,3}$ for amide I-III cross peak and $\eta_{3,4}$ for amide I-A cross peak). As the correlation of the fundamental fluctuations is varied from +1 to -1, the negative peak intensity becomes weaker in the $\text{Im}[S_i(-\omega_1, t_2=0, \omega_3)]$ signal and becomes stronger in $\text{Im}[S_{iii}(-\omega_1, t_2=0, \omega_3)]$. The positive peaks of $\text{Im}[S_i(-\omega_1, t_2=0, \omega_3)]$ and $\text{Im}[S_{iii}(-\omega_1, t_2=0, \omega_3)]$ are sensitive to the correlation between the fundamental and the combination frequency fluctuations ($\eta_{1,9}$ for I-III cross peaks and $\eta_{3,13}$ for I-A cross peaks). As the correlation of the fundamental and the combination fluctuations is varied from +1 to -1, the positive peak intensity becomes decreased in $\text{Im}[S_i(-\omega_1, t_2=0, \omega_3)]$ and increased in $\text{Im}[S_{iii}(-\omega_1, t_2=0, \omega_3)]$. The elongation of the positive band shape also changes significantly as the two correlations change. The changes of the negative peak in \mathbf{k}_i signal is in agreement with the earlier model study of two coupled vibrations interacting with a

Brownian oscillator bath³² in the intermediate bath region. The actual simulation of amide I-III cross peaks (anticorrelated $\eta_{1,3}$ and correlated $\eta_{1,9}$) gives weaker signals than both full correlated in \mathbf{k}_i signal ($\text{Im}[S_i(-\omega_1, t_2=0, \omega_3)]$) and stronger signals in \mathbf{k}_{iii} signal ($\text{Im}[S_{iii}(-\omega_1, t_2=0, \omega_3)]$). Correlated $\eta_{3,4}$ and $\eta_{3,13}$ in actual simulation enhance the negative and positive peaks of $\text{Im}[S_i(-\omega_1, t_2=0, \omega_3)]$. $\text{Im}[S_{iii}(t_1=0, \omega_2, \omega_3)]$ signal is sensitive to the correlations of the combination frequency with its fundamental fluctuations. The amide I-III (I-A) negative peak intensity becomes stronger as $\eta_{3,9}$ ($\eta_{4,13}$) is varied from +1 to -1. The amide I-III (I-A) positive peak intensity becomes weaker as $\eta_{1,9}$ ($\eta_{3,13}$) is varied from +1 to -1.

In order to establish the connection between the correlation of the amide fluctuations and the hydrogen-bond dynamics, hydrogen-bond configurations were classified by employing the geometric criteria. The number of hydrogen bonds at C=O and N-H is positive correlated (0.673). This can be ascribed to an extra stabilization energy (0.03 kcal/mol) when both hydrogen bonds at C=O and N-H are formed which was obtained from the equilibrium populations of the six H-bond species; the hydrogen bond at one site creates the electric field parallel to the C=O or N-H bond, which stabilizes the other hydrogen bond.

The amide fundamental fluctuations are connected with different hydrogen bonds. The amide I fundamental is sensitive exclusively to the hydrogen bond to C=O, and amide A depends on the hydrogen bond at N-H. The amide II and III frequencies are also more sensitive to N-H. The amide I and A fundamental fluctuations are positively correlated with the number of hydrogen bonds at C=O and N-H, respectively. The amide III frequency is anticorrelated with hydrogen bonds at N-H. The positive correlation between amide I and A frequencies (0.16) and negative correlation between amide I and III frequencies (-0.76) can be ascribed to the correlated H-bond dynamics at C=O and N-H. The global reorientation of solvent is also found to be important (24%–63%) to the solvent shifts of amide III, I, and A.

In our earlier study, we examined the correlation between the C=O and N-H bond lengths and their correlations with amide frequencies (Figs. 7 and 9 of Ref. 29). The C=O and N-H bond lengths are positively correlated. The amide I and A frequencies are anticorrelated with C=O and N-H bond lengths, respectively. Amide II and III frequencies are positively correlated with N-H bond length. A possible mechanism is as follows. The hydrogen bond at N-H makes the N-H bond length longer. The longer N-H bond length weakens the N-H bond, redshifting the amide A frequency (N-H stretch), which causes the negative correlations of the amide A frequency to N-H bond length and to hydrogen bonds at N-H. The H bonding at N-H also stabilizes more

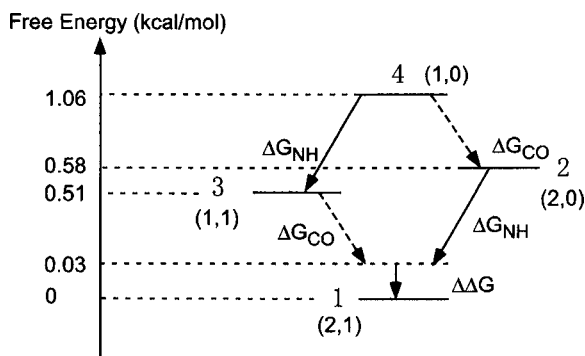


FIG. 11. Free energy diagram of the four major hydrogen bonding configurations (1–4). The additional stabilization energy due to the simultaneous hydrogen bondings on both C=O and N-H sites ($\Delta\Delta G$) is calculated to be 0.03 kcal/mol.

the parallel N–H···OH₂ structure, blueshifting the bending modes (amide II and III), resulting in the positive correlations of the amide II and III modes to N–H bond length and to H bonds at N–H. On the other hand, H bond at C=O makes the C=O bond length longer, redshifting the amide I frequency (C=O stretch) which causes the negative correlations of the amide I frequency to C=O bond length and to hydrogen bonds at C=O. The correlated H-bond dynamics at C=O and N–H causes the correlated C=O and N–H bond lengths, correlated amide I and A fundamental fluctuations, and anticorrelated amide I and III fundamental fluctuations.

ACKNOWLEDGMENTS

We thank Wei Zhuang for useful discussions and critical comments. The support of the National Institutes of Health Grant No. RO1 GM059230-05 and the National Science Foundation Grant No. CHE-0446555 is gratefully acknowledged.

- ¹J. B. Asbury, T. Steinel, C. Stromberg, K. J. Gaffney, I. R. Piletic, A. Goun, and M. D. Fayer, *Chem. Phys. Lett.* **374**, 362 (2003).
- ²J. Bredenbeck and P. Hamm, *J. Chem. Phys.* **119**, 1569 (2003).
- ³M. Khalil, N. Demirdoven, and A. Tokmakoff, *J. Phys. Chem. A* **107**, 5258 (2003).
- ⁴A. T. Krummel, P. Mukherjee, and M. T. Zanni, *J. Phys. Chem. B* **107**, 9165 (2003).
- ⁵S. Woutersen, R. Pfister, P. Hamm, Y. Mu, D. S. Kosov, and G. Stock, *J. Chem. Phys.* **117**, 6833 (2002).
- ⁶O. Golonzka, M. Khalil, N. Demirdoven, and A. Tokmakoff, *Phys. Rev. Lett.* **86**, 2154 (2001).
- ⁷D. E. Thompson, K. A. Merchant, and M. D. Fayer, *J. Chem. Phys.* **115**, 317 (2001).
- ⁸S. Woutersen and P. Hamm, *J. Chem. Phys.* **115**, 7737 (2001).
- ⁹S. Woutersen and P. Hamm, *J. Chem. Phys.* **114**, 2727 (2001).
- ¹⁰M. T. Zanni, M. C. Asplund, and R. M. Hochstrasser, *J. Chem. Phys.* **114**, 4579 (2001).
- ¹¹A. Piryatinski, S. Tretiak, V. Chernyak, and S. Mukamel, *J. Raman Spectrosc.* **31**, 125 (2000).
- ¹²K. A. Merchant, W. G. Noid, R. Akiyama, I. J. Finkelstein, A. Goun, B. L. McClain, R. F. Loring, and M. D. Fayer, *J. Am. Chem. Soc.* **125**, 13804 (2003).
- ¹³Y. Tanimura and S. Mukamel, *J. Chem. Phys.* **99**, 9496 (1993).
- ¹⁴P. Hamm, M. H. Lim, and R. M. Hochstrasser, *J. Phys. Chem. B* **102**, 6123 (1998).
- ¹⁵C. Scheurer and S. Mukamel, *Bull. Chem. Soc. Jpn.* **75**, 989 (2002).
- ¹⁶C. M. Cheatum, A. Tokmakoff, and J. Knoester, *J. Chem. Phys.* **120**, 8201 (2004).
- ¹⁷N. Demirdoven, C. M. Cheatum, H. S. Chung, M. Khalil, J. Knoester, and A. Tokmakoff, *J. Am. Chem. Soc.* **126**, 7981 (2004).
- ¹⁸A. M. Moran, S.-M. Park, and S. Mukamel, *J. Chem. Phys.* **118**, 9971 (2003).
- ¹⁹D. G. Covell and A. Wallqvist, *J. Mol. Biol.* **269**, 281 (1997).
- ²⁰H. F. Xu and B. J. Berne, *J. Phys. Chem. B* **105**, 11929 (2001).
- ²¹L. Hua, X. H. Huang, R. H. Zhou, and B. J. Berne, *J. Phys. Chem. B* **110**, 3704 (2006).
- ²²T. Mirshahi, D. E. Logothetis, and A. Rosenhouse-Dantsker, *Biophys. J.* **90**, 2776 (2006).
- ²³I. V. Rubtsov, J. Wang, and R. M. Hochstrasser, *J. Chem. Phys.* **118**, 7733 (2003).
- ²⁴I. V. Rubtsov, J. Wang, and R. M. Hochstrasser, *Proc. Natl. Acad. Sci. U.S.A.* **100**, 5601 (2003).
- ²⁵N. A. Besley, *J. Phys. Chem. A* **108**, 10794 (2004).
- ²⁶M. Cho, *J. Chem. Phys.* **118**, 3480 (2003).
- ²⁷S. Ham, J. H. Kim, H. Lee, and M. H. Cho, *J. Chem. Phys.* **118**, 3491 (2003).
- ²⁸P. Bour, D. Michalik, and J. Kapitan, *J. Chem. Phys.* **122**, 144501 (2005).
- ²⁹T. Hayashi, W. Zhuang, and S. Mukamel, *J. Phys. Chem. A* **109**, 9747 (2005).
- ³⁰T. Hayashi, T. I. C. Jansen, W. Zhuang, and S. Mukamel, *J. Phys. Chem. A* **109**, 64 (2005).
- ³¹P. DeFlores, Z. Ganim, S. F. Ackley, H. S. Chung, and A. Tokmakoff, *J. Phys. Chem. B* **110**, 18973 (2006).
- ³²R. Venkatramani and S. Mukamel, *J. Chem. Phys.* **117**, 11089 (2002).
- ³³A. D. Becke, *Phys. Rev. A* **38**, 3098 (1988).
- ³⁴M. J. Frisch, G. W. Trucks, H. B. Schlegel *et al.*, GAUSSIAN 03, Revision C.02, Gaussian, Inc., Pittsburgh, PA, 2003.
- ³⁵S. Patel, A. D. Mackerell, and C. L. Brooks, *J. Comput. Chem.* **25**, 1504 (2004).
- ³⁶S. Mukamel, *Principles of Nonlinear Optical Spectroscopy* (Oxford University Press, New York, 1995).
- ³⁷S. Mukamel and D. Abramavicius, *Chem. Rev. (Washington, D.C.)* **104**, 2073 (2004).
- ³⁸C. P. Lawrence and J. L. Skinner, *J. Chem. Phys.* **118**, 264 (2003).
- ³⁹A. Luzar and D. Chandler, *Nature (London)* **379**, 55 (1996).
- ⁴⁰F. Csajka and D. Chandler, *J. Chem. Phys.* **109**, 1125 (1998).
- ⁴¹H. Guo and M. Karplus, *J. Phys. Chem.* **96**, 7273 (1992).